journal

J. Am. Ceram. Soc., 98 [10] 3270–3279 (2015)
DOI: 10.1111/jace.13774

MnO_2 Thin Film Electrodes for Enhanced Reliability of Thin Glass Capacitors

Betul Akkopru-Akgun,[‡,§,†] Susan Trolier-McKinstry,[‡,§] and Michael T Lanagan[‡,¶]

[‡]Center for Dielectrics and Piezoelectrics, Materials Research Institute, The Pennsylvania State University, University Park, Pennsylvania 16802

[§]Department of Materials Science and Engineering, The Pennsylvania State University, University Park, Pennsylvania 16802

[¶]Department of Engineering Science and Mechanics, The Pennsylvania State University, University Park, Pennsylvania 16802

Many dielectric thin films for energy storage capacitors fail by thermal breakdown events under high-field drive conditions. The lifetime of the device can be improved under conditions where the current path within the defect regions in dielectrics is eliminated. Self-healing electrodes were developed by depositing a manganese dioxide (MnO_2) thin film between the glass substrate and an aluminum film. For this purpose, thin films of MnO_2 on boroaluminosilicate glass were fabricated via chemical solution deposition and heat-treated at temperatures in the range 500°C–900°C. The α-MnO_2 structure was stabilized by Ba^{2+} insertion to form the hollandite structure. The phase transition temperature of α-MnO_2 to Mn_2O_3 is strongly dependent on the Ba concentration, with transition temperatures of 600°C and 675°C with Ba concentrations of [Ba]/[Mn] = 0.04 and 0.1, respectively. The electrical resistivity increased from 4.5 Ω·cm for MnO_2 to 10^5 Ω·cm for Mn_2O_3. Both dielectric breakdown strength and the associated cleared aluminum electrode area increased with an MnO_2 interlayer between Al electrodes and the borosilicate glass. The enhancement in dielectric strength was related with self-healing. The associated redox reaction between MnO_2 and Mn_2O_3 was also proved by RAMAN spectroscopy following dielectric breakdown.

I. Introduction

There has been increasing demand to develop reliable high energy density dielectrics for capacitors. High energy density dielectrics are utilized in power electronics and pulsed power applications to mitigate the problems associated with the size, temperature stability, and reliability of the energy storage devices. One approach to achieve the desired properties in energy storage devices is to enhance the energy density and power density of the dielectric materials.[1–5] The amount of electrostatic energy that can be stored in a dielectric is strongly dependent on the dielectric constant and breakdown strength of the material. For a linear dielectric material, the energy density varies as,[6]

$$U_e = \frac{1}{2}\varepsilon_0\varepsilon_r E_b^2 \quad (1)$$

where U_e is energy storage density, ε_0 is the vacuum permittivity, ε_r is the dielectric permittivity, and E_b is the dielectric breakdown strength in the dielectric. Thus high dielectric constants coupled with high breakdown strengths are essential to significantly increase energy density.[7] A number of polymers such as polypropylene have an advantage over other dielectrics because they possess high electric breakdown field and graceful failure.[8,9] However, the low dielectric constant and low-temperature stability of polymers limit their application in high energy density capacitors operated under high electric fields.[10] In contrast, dielectric ceramics show much higher dielectric constant and improved temperature stability, but their low breakdown field strength (originating from microstructural defects such as pores and secondary phases) results in low energy density.[11,12]

Development of new dielectric materials is essential to simultaneously achieve high permittivity with high dielectric breakdown strength under high electric field and temperature. In recent years, glass and glass-ceramics have been found to be promising for high energy density applications due to substantially higher breakdown strength than polycrystalline ceramics and the potential for graceful failure.[13] Alkali-free glass sheets have superior dielectric breakdown strengths exceeding 12 MV/cm and an electrostatic energy density of approximately 38 J/cm^3, while maintaining a low dielectric loss up to moderate temperatures around 200°C.[13–15]

Breakdown in glasses is generally related to accumulation of high-mobility charges at defect sites or microstructural inhomogeneities and has different contributions, including thermal, electrical, and mechanical.[16] Thermal breakdown occurs when Joule heating produced from conduction or dielectric loss cannot be dissipated fast enough by the glass, which leads to an increase in conductivity and temperature, and eventually catastrophic failure of the dielectric.[16] Avalanche breakdown on the other hand is mostly associated with current injection from the cathode to the conduction band. These energetic electrons ionize other atoms to produce more electrons until conduction occurs through the material.[16] The dielectric breakdown strength, E_B, of glass is dramatically affected by the dielectric thickness;[17] E_B was reported to be 12 MV/cm for a 5 μm boroaluminosilicate glass while in a 50 μm thickness of the same material E_B decreased to 4 MV/cm.[15] The improvement in dielectric breakdown strength is partially due to an increase in heat transfer to the ambient environment with decrease in dielectric layer thickness. The thickness-dependent breakdown is caused by alkali migration and internal field enhancement. High current is subsequently generated and the local temperature rises. In addition, the probability of finding critical defect concentrations to initiate dielectric breakdown decreases, as the dielectric layer becomes thinner.[13]

The pore size and pore distribution was also shown to affect the breakdown strength of dielectrics. When the volume percentage porosity throughout the dielectric exceeded 10%, the dielectric breakdown strength was found to decrease to one-half of the intrinsic value.[18]

The dielectric breakdown in glass is catastrophic and thus leads to formation of either physical cracks or/and melted

G. L. Brennecka—contributing editor

Manuscript No. 36172. Received December 31, 2014; approved June 23, 2015.
†Author to whom correspondence should be addressed.
e-mail: betul.akkopru@gmail.com

regions at the breakdown site, preventing that spot from performing successfully as a dielectric. Many studies have been carried out to prevent catastrophic damage of devices during dielectric breakdown, allowing for uninterrupted operation of the capacitor in high-field applications (>10^8 V/m).[19] Special electrodes were designed that either undergo a phase change or are consumed during a dielectric breakdown event, thus limiting leakage current at the breakdown site. This approach is widespread in tantalum capacitors, as will be described below.[20] As a result, the capacitor remains operational with only a slight decrease in the capacitance value. The concept of a vaporizing or causing a phase change in the electrode material is known as graceful failure or self-healing.

Self-healing based on evaporation of metal electrode has been observed for inorganic, polymer, and electrolytic capacitors with aluminum electrodes.[8,20,21] Aluminum electrodes have relatively low melting and evaporation temperatures. When the heat dissipated in the fault region is sufficient to evaporate the aluminum electrode, it can eliminate conduction at a fault site, which prevents formation of an open circuit. Consequently, the lifetime of the device is improved by removing the failed portion from the circuit.[8,21,22] The primary condition of self-healing process is that the electrostatic energy released in the fault regions is sufficient to evaporate the aluminum electrodes.[22] Thus, the thickness of the aluminum electrodes is a key parameter in developing metallized capacitors; thicknesses less than 2000 Å have been reported to enable graceful failure.[8]

The propensity for self-healing is related to the cleared electrode volume and is correlated with the stored electrostatic energy and latent heat of vaporization for the electrode material as defined by Eq. (2).[19] The values, q_m and V_m are the heat-of-vaporization and the evaporated metal volume, respectively. The dissipated energy during dielectric breakdown is represented by the left side of Eq. (2).[19]

$$\left(\frac{CV_B^2}{2}\right)\left[\frac{2R_m}{(2R_m + R_i)}\right] = 2q_m V_m \quad (2)$$

The total energy dissipated during breakdown is related to the capacitance of the local breakdown region [C in Eq. (2)] and the breakdown voltage, V_B. Joule heating occurs from the discharge current though the metal (R_m) and insulator (R_i).[19]

The left side of Eq. (2) contains the total electrostatic energy available in terms of the capacitance and voltage. The capacitance is not necessarily the device capacitance, but it is related to the available charge within the spatial and time limitations of the breakdown event. Typically, the value of the capacitance is limited by the area near the defect. The energy delivered by the local capacitance is partitioned between the metal and insulator through the respective resistances. From Eq. (2), it would be desirable to have a high metal resistivity; however, the metal resistivity is related to the overall equivalent series resistance of the device. In this work, a MnO_2 interlayer between the dielectric and a low resistance Al layer enables low metal resistance and provides an additional mechanism for electrode clearing.

The use of self-healing electrodes that evaporate at the fault site during breakdown has some limitations because they can only be applied to single layer devices. In multilayer devices, destructive removal of the electrode may produce catastrophic damage elsewhere. In addition, the residues after evaporation of the electrode may have sufficient conductivity to initiate subsequent failure events. Consequently, it would be desirable to build in a graceful failure mechanism through an electrode which undergoes a phase change from an electrical conductor to an electrical insulator after reaching a critical threshold temperature. This type of graceful failure mechanism is expected to be particularly important in parts which either utilize glass as the dielectric layer, or as the substrate for the active layer, as the thermal conductivity of glass is quite low.

Manganese dioxide is a good candidate for a self-healing electrode material due to its low cost, low toxicity, and environmental safety.[23,24] MnO_x is widely used in tantalum electrolytic capacitors,[20] where the self-healing mechanism is based on redox reactions in the MnO_2 electrode. That is, when the dielectric begins to conduct current at defective regions, the current flow results in Joule heating. Localized heating of the MnO_2 electrodes converts the MnO_2 to an insulating Mn_2O_3 phase. Formation of the Mn_2O_3 phase dramatically increases the resistivity of the electrode material, restricting the current flow through the defect sites, which prevents the whole system from catastrophic damage by making an open circuit.[20,25] In addition, the exothermic reaction and availability of oxygen to the aluminum conductor will promote electrode clearing. The primary requirement for self-healing is sufficient current flow for the conversion of conducting MnO_2 to insulating Mn_2O_3. Here, MnO_2 thin film electrodes for high-temperature high energy density glass capacitors were explored for use as a self-healing electrode to increase the reliability of the dielectric.

MnO_2 exists in a diversity of polymorphs. The desired (micro)structural properties to improve the self-healing mechanism are; (1) high specific surface area, providing more active sites for the redox reaction between the Mn^{3+} and Mn^{4+}, (2) high electrical conductivity to increase charge transport and, (3) high mechanical stability.[26] The preferred physical and structural properties of MnO_2 electrodes can be obtained by optimizing processing parameters or/and production methods. Numerous preparation methods have been employed to deposit MnO_2 thin films, including chemical vapor deposition,[27] sol–gel synthesis,[28] atomic layer deposition,[29] electrodeposition,[30] and sputtering.[31] Although a number of studies have been conducted on synthesis of MnO_2 thin films, controlled synthesis of stoichiometric MnO_2 with high purity and chemical stability is problematic due to the small stability region of MnO_2 in the Mn–O phase diagram and hence the possibility of crystallization in different polymorphs.

In this study, self-healing MnO_2 film electrodes were deposited on thin boroaluminosilicate glasses using spin coating of a sol–gel solution. The objective of this study was to explore physical and structural properties enabling graceful failure for glass capacitors. The dependence of the MnO_2 crystal structure on heat-treatment temperature and changes in chemical nature and stability of MnO_2 by thermal treatments were investigated. Special emphasis was given to the correlation between the stability of the MnO_2 structure and the electrical properties. Another specific objective was to determine the change in dielectric breakdown behavior of thin boroaluminosilicate glasses after coating with MnO_2 thin film electrodes.

II. Experimental Procedure

(1) Sol Preparation

Mn_xO_y-based solutions were prepared from manganese (II) acetate tetrahydrate [$(CH_3COO)_2Mn{\cdot}4H_2O$ or MnAC, Sigma-Aldrich, St. Louis, MO], acetic acid (CH_3CO_2H, Sigma-Aldrich), 2-methoxyethanol ($CH_3OCH_2CH_2OH$- or 2-MEO, Sigma-Aldrich), barium acetate $(CH_3COO)_2Ba$ or BaAC, Sigma-Aldrich) and, DI (deionized water). Four different sols were prepared with [BaAC]/[MnAC] molar ratios of 0.0, 0.4, 1.0, and 1.5. First 1 g manganase (II) acetate tetrahydrate was dissolved in DI water and then 17.4*M* acetic acid was added dropwise into the solution until the pH reached a value of 5.[6] The resultant $MnAC/CH_3CO_2H/H_2O$ mixture (which will be referred to as Solution-A), was then stirred for 60 min. In a separate beaker, a $(CH_3COO)_2Ba/H_2O/CH_3CO_2H$ solution was prepared and stirred at 25°C for 60 min to form Solution-B. The [BaAC]:

Table I. Formulations of Coating Solutions

[BaAC]/[MnAC] molar ratio	MnAC	BaAC	H_2O	2MOE	CH_3CO_2H
[BaAC]/[MnAC] = 0.0	0.02	0.00	0.54	1.00	0.34
[BaAC]/[MnAC] = 0.4	0.02	0.008	0.54	1.00	0.34
[BaAC]/[MnAC] = 0.1	0.02	0.02	0.54	1.00	0.34
[BaAC]/[MnAC] = 0.04	0.02	0.03	0.54	1.00	0.34

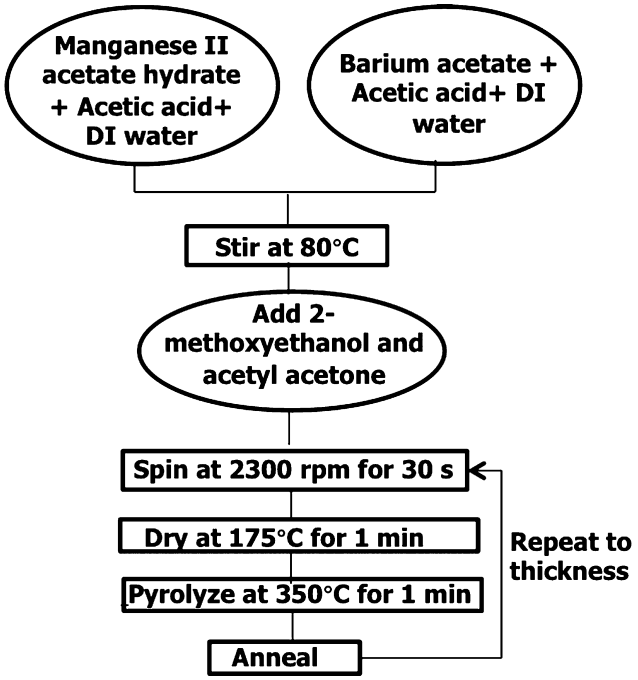

Fig. 1. Flowchart for the processing of barium-stabilized Mn_xO_y thin films. Solutions were prepared using a sol–gel method, spin cast onto a substrate, and thermally treated in three steps.

[MnAC] molar ratios and final thin film solution molar ratios are given in Table I. Finally, Solution-B was slowly added into Solution-A while stirring; the resulting solution was subsequently mixed for 180 min at 25°C. The final pH value was 6.[25] At the end, a clear and precipitate-free aqueous thin film sol was obtained, which did not show any color change up to 1 month after preparation. Typically, thin film sols were aged for 2 d prior to coating.

(2) Preparation of Thin Films

Two types of substrates (1) Ba-boroaluminosilicate glass and (2) an SiO_2/Si wafer were used. As the glass substrates were very thin (50 μm), the SiO_2/Si wafer was used for the experiments designed for optimization of structural properties, which are desired for high self-healing performance of MnO_2 electrodes. Electrode clearing studies were carried out on the AF45 boroaluminoslicate glass. The substrates were 2.5 cm × 2.5 cm in size. Prior to coating, both type of substrates were exposed to rapid thermal processing at 600°C for 2 min to remove surface moisture. The Mn_xO_y-based thin films were prepared via spin coating. First 0.5 mL of solution was dispensed onto the substrate through a 0.1 μm polytetrafluoroethylene (Restek Corporation, Bellefonte, PA) syringe filter. Then a single layer was spun at 2300 rpm for 30 s. The resultant samples were first dried in air at 150°C for 1 min and then pyrolyzed at 300°C for 2 min. This will be referred to as the "as-prepared" condition for the thin films. As-prepared thin films were heat-treated under an O_2 atmosphere at temperatures from 500°C to 900°C for 5 min using rapid thermal processing. The coating and drying process, as well as rapid thermal treatments were repeated 10 times to obtain thin films with the desired thickness. The resultant film thickness is 350 ± 40 nm. The flowchart for the processing of Mn_xO_y films is given in Fig. 1.

(3) Materials Characterization

A series of characterization tools were employed to assess the morphology, thickness, and structure of the films. In particular, the film surface morphology was determined using field-emission scanning electron microscopy (Leo 1530; LEO Electron Microscopy Ltd., Cambridge, England) operated at 5.00 kV for secondary electron imaging. The film thickness was measured using a profilometer (Alpha-Step 500 Surface Profilometer, Tencor, Portsmouth, NH). The phase and crystallinity of the films were determined by Grazing Incidence X-ray diffraction (GIXRD) analysis (X'Pert Pro MPD,; PANalytical, Almelo, The Netherlands). The X-ray source was CuK_α radiation at 40 kV. The step size and hold time at each step was 0.02° and 0.5 s, respectively. X-ray diffraction patterns were collected between 15° and 70° 2θ.

For electric characterizations, Pt top electrodes, approximately 1000 Å in thickness with diameters of 1 mm were sputtered onto the film through a shadow mask. The Pt top electrodes were sputtered in an Ar plasma at room temperature using a power density of 2 W/cm^2 and working pressure of 2.5 mtorr. (CMS-18 Sputter System, Kurt J. Lesker Company, Pittsburgh, PA). Electrical resistivity measurements were made by the Van der Pauw method, employing an HP E3612A (Keysight Technologies, Santa Rosa, CA) DC power supply and digital multimeters at temperatures ranging from room temperature to 750°C.

The dielectric breakdown strength of MnO_2-coated glass and uncoated glass was measured at room temperature. To measure the breakdown voltage, a high-voltage power supply was used to generate a 500 V/s ramp waveform. The samples were immersed in perfluoropolyether fluid (Sigma-Aldrich) to prevent arcing occurs in the surrounding air. Aluminum-coated polypropylene was placed either on bare glass or on MnO_2-coated glass substrates to make electrical contact to either side of the glass. The PP/aluminum film was attached to the electrical system in a position that is far away from the breakdown region of interest. This is because any point

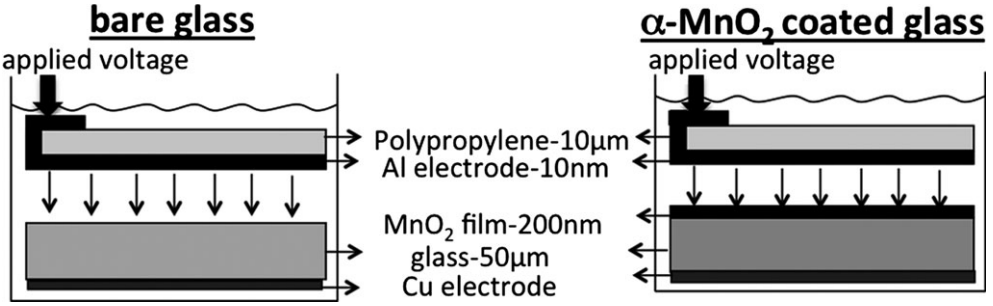

Fig. 2. Schematic representation of breakdown apparatus used in this study. Electrostatic forces (depicted as arrows) pull the top electrode down to the glass and MnO_2-coated glass surface.

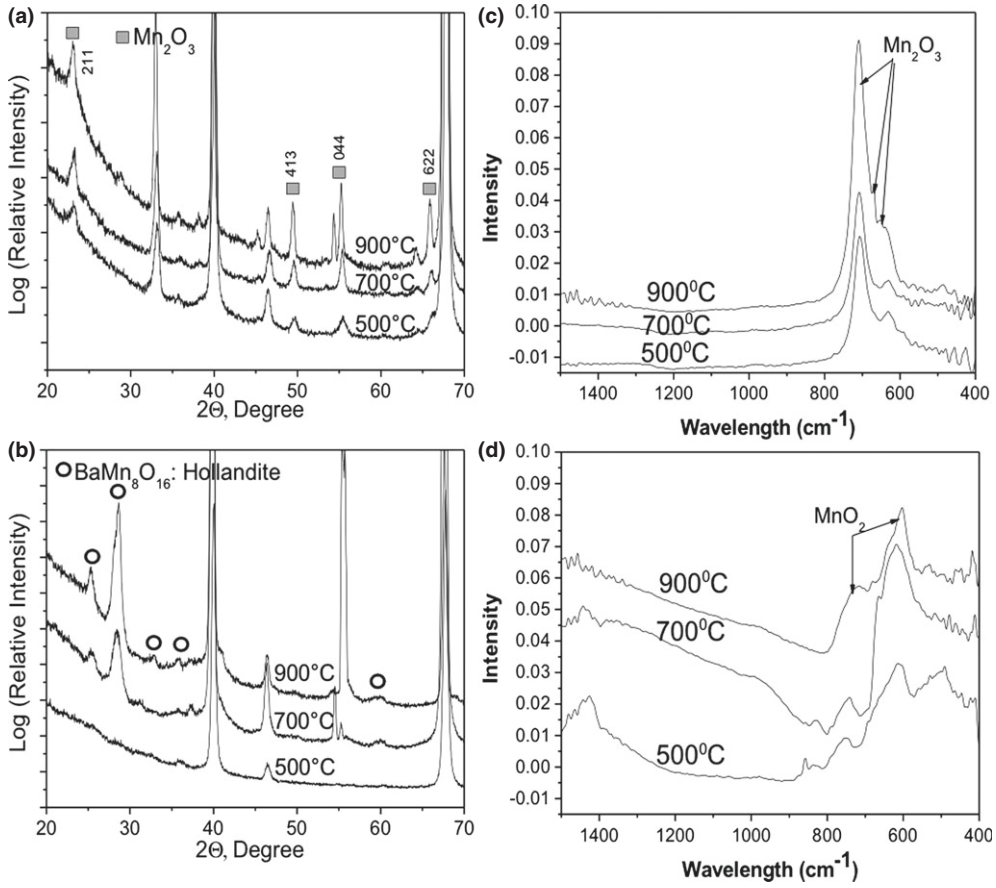

Fig. 3. XRD diffraction patterns of (a) pure ([BaAC]/[MnAC] = 0.0) and (b) barium-doped manganese oxide film ([BaAC]/[MnAC] = 0.4) after heat-treatment at 500°C, 700°C, and 900°C. FTIR spectra of (c) pure ([BaAC]/[MnAC] = 0.0) and (d) barium-doped manganese oxide film ([BaAC]/[MnAC] = 0.4) after heat-treatment at 500°C, 700°C, or 900°C.

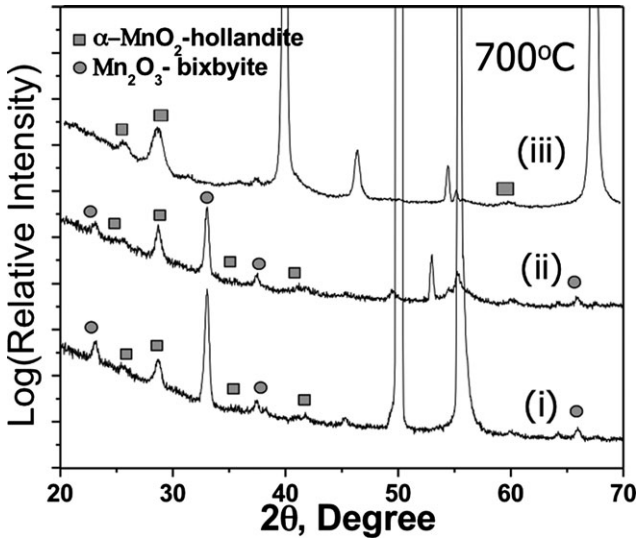

Fig. 4. XRD diffraction patterns of barium-doped manganese oxide films with different Ba concentrations ((i) [BaAC]/[MnAC] = 0.04, (ii) [BaAC]/[MnAC] = 0.1, and (iii) [BaAC]/[MnAC] = 0.4) after heat-treatment at 700°C.

probes near the breakdown area will cause high current density with additional evaporation that is not associated with the breakdown energy.

The breakdown apparatus used in this study is depicted schematically in Fig. 2. The field was applied to the Al electrode and then the voltage was increased at the rate of 500 V/s until breakdown occurred, whereas the current was recorded as a function of time. After the breakdown, the aluminum-coated polypropylene film was separated from the glass substrate and was imaged using an optical microscope to quantify the area and composition of the cleared electrode region. The cleared electrode area represents the regions of vaporized or insulating electrode around the punch-through region upon the breakdown process. The area near the cleared region was investigated to find out whether the MnO_2 to Mn_2O_3 phase transformation occurred as a result of the heat dissipated near the breakdown region. For this purpose, a WiTec Confocal CRM 200 (WiTec, Ulm, Germany) Raman microscope/spectrometer with a 488 nm laser 25 mW excitation was used. The spectra were collected from 100 to 1800 cm^{-1}.

III. Results and Discussion

(1) Phase Identification and Film Structure

The X-ray diffraction patterns of pure and Ba-doped manganese oxide films after heat-treatment at 500°C, 700°C, and 900°C are shown in Figs. 3(a) and (b). Pure manganese oxide films heat-treated at 500°C show the formation of a Mn_2O_3 (bixbyite, PDF 01-071-0635) phase. This is consistent with the phase diagram of manganese oxides[32] for 500°C and 10 mTorr O_2(g). That is, the Mn^{2+} ions in the precursor solution oxidize to Mn^{3+} to form Mn_2O_3 (bixbyite) when exposed to heat-treatment at 500°C in an O_2 atmosphere. The intensity of bixbyite peaks increases for the thin film samples heat-treated at 700°C and 900°C. In agreement, the IR spectra of pure manganese oxide thin films [Fig. 3(c)] displayed three main bands at 633, 537, and 415 cm^{-1} in the region 1000–4000 cm^{-1}, similar to those at 602, 533, and 408 cm^{-1}, reported for the bixbyite phase.[33]

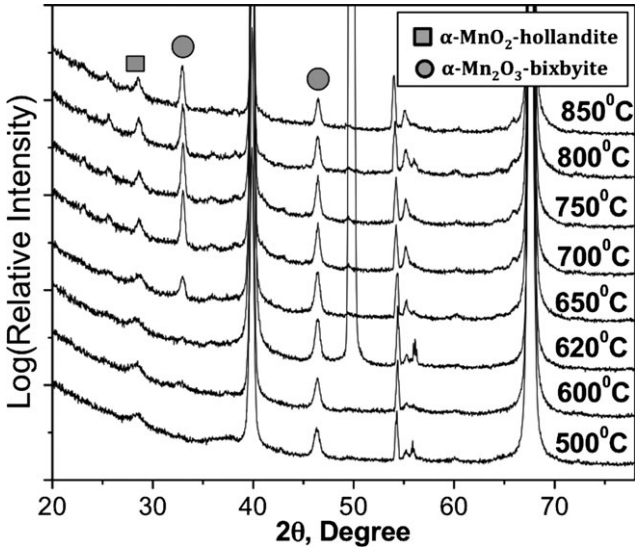

Fig. 5. GIXRD diffraction patterns of Ba-doped manganese oxide films ([BaAC]/[MnAC] = 0.04) after heat-treatment at 500°C, 600°C, 620°C, 650°C, 700°C, 750°C, 800°C, 850°C.

The addition of barium ([BaAC]/[MnAC] = 0.4) results in a disappearance of bixbyite peaks in films heat-treated at 500°C, accompanied by emergence of weak α-MnO_2 (hollandite, PDF 00-029-0188, $BaMn_8O_{16}$) peaks at 28.7° and 37.2°, corresponding to early stages of hollandite phase formation [Fig. 3(b)]. Stabilization of α-MnO_2 has previously been reported when Ba^{2+} cations occupy the (2 × 2) or (1 × 1) channels of the hollandite structure.[34] The α-MnO_2 (hollandite) structure consists of edge or corner-shared MnO_6 octahedra. These octahedra are arranged to form (2 × 2) openings. In pure MnO_2, these openings can accommodate H_3O^+ ions; these are easily removed from the structure upon thermal treatment.[35] As a result, the structure collapses easily at elevated temperature.[34,35] On the other hand, the channels in Ba-doped MnO_2 films are occupied by Ba^{2+} ions. The addition of a Ba^{2+} to MnO_2 reduces two Mn^{4+} to Mn^{3+}. The extra electrons are initially located on a single Mn, resulting in the Jahn–Teller distortion typical for Mn^{3+} ions. With the ions frozen in this position, the state with a localized electron is found to be electronically stable.[36] The tunnel structure of α-MnO_2 becomes stable even at high temperature, preventing oxygen release and reduction in Mn ions. For this Ba concentration, the MnO_2 structure remains stable even after heat-treatment temperature at 700°C or 900°C, as shown in Figs. 3(b) and (d).

Phase transformation of pure MnO_2 to the high-temperature Mn_2O_3 phase occurs in the temperature range 500°C–600°C.[32] However, it has been reported that the phase transition temperature shifts above 800°C after addition of Ba into the MnO_2.[25] For the thin films with [BaAC]/[MnAC] = 0.4, the X-ray peak intensity increases with crystallization temperature to 900°C. After heat-treatment at 700°C and 900°C, the intensity of XRD peaks at 28.7° and 37.2°, corresponding to MnO_2 becomes more intense, accompanied by emergence of new MnO_2 peaks at 36.5° and 59.6° [Fig. 3(b)]. The stabilization of the α-MnO_2 structure in Ba-doped thin films is also supported via IR results. For thin films with [BaAC]/[MnAC] = 0.4, two well-resolved bands can be distinguishable at 611 and 744 cm^{-1}, corresponding to Mn–O stretching vibrations of α-MnO_2, were detected after heat-treatment at 500°C [Fig. 3(d)].[37] As the heat-treatment temperature

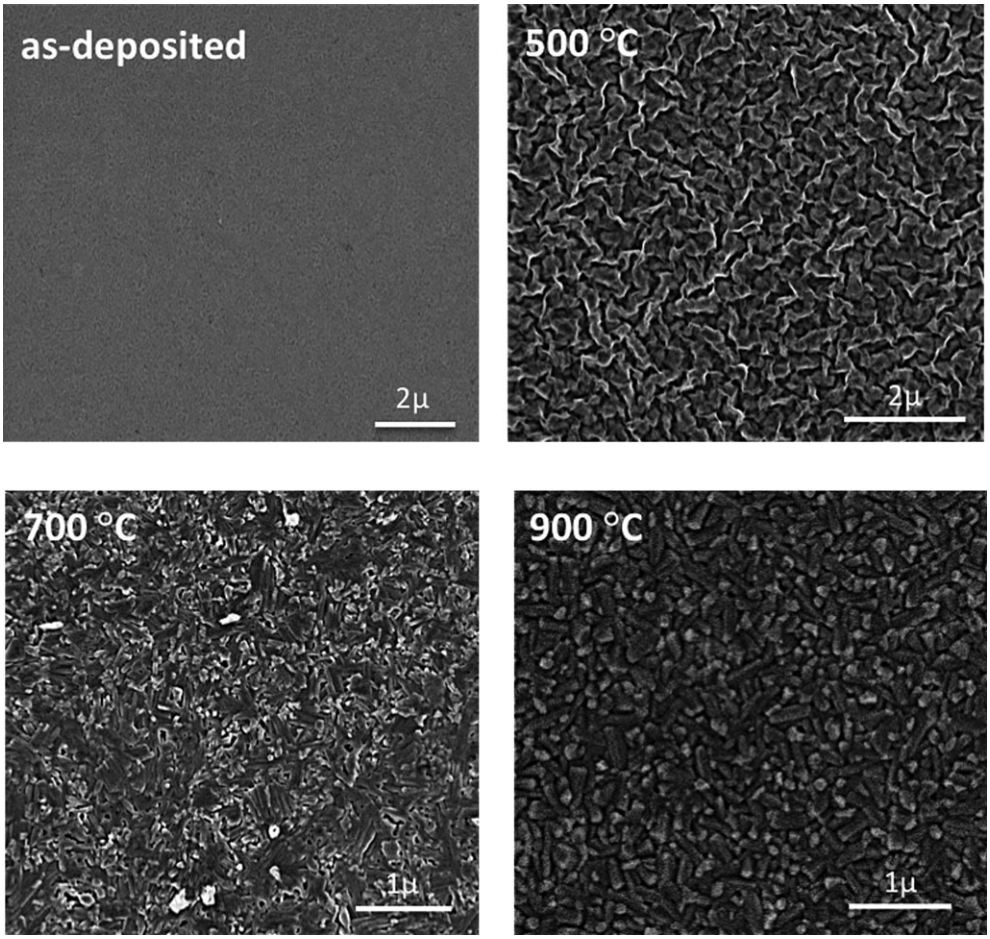

Fig. 6. FESEM micrographs of Ba-doped manganese oxide films ([BaAC]/[MnAC] = 0.04) after heat-treatment at 500°C, 700°C, and 900°C.

Table II. Electrical Properties of Ba-doped Manganese Oxide Films

	Resistivity (Ω·cm)	Activation energy (eV)
[BaAC]/[MnAC] = 0.04		
500°C	103.1 ± 10	0.81 ± 0.15
700°C	20.2 ± 4	0.34 ± 0.1
[BaAC]/[MnAC] = 0.1		
500°C	44.7 ± 5	0.44 ± 0.15
700°C	18.8 ± 4	0.31 ± 0.1
[BaAC]/[MnAC] = 0.4		
500°C	9.8 ± 3	0.24 ± 0.08
700°C	5.5 ± 1.5	0.18 ± 0.06
900°C	4.2 ± 0.8	0.12 ± 0.05

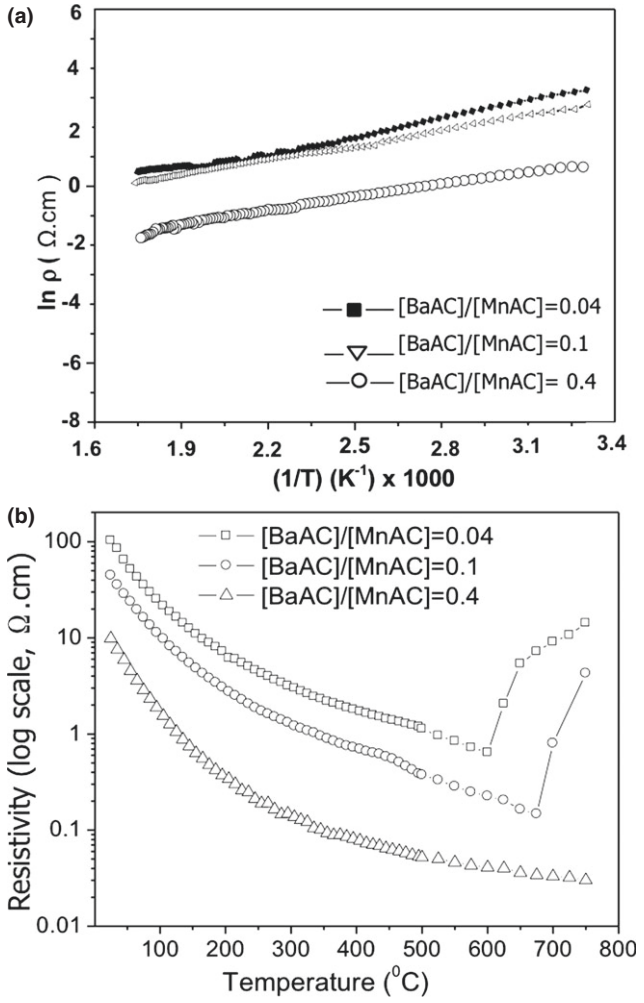

Fig. 7. (a) Temperature dependence of electrical resistivity and corresponding activation energy fits, and (b) The electrical resistivity dependence on annealing temperature for Ba added manganese oxide films with different Ba contents.

increases to 700°C and 900°C, the same MnO_2 vibrational bands appear stronger and narrower, suggesting that the α-MnO_2 phase remains stable.

The phase stability of α-MnO_2 and phase transition temperature to insulating Mn_2O_3 is strongly dependent on the initial Ba concentration. As was shown above, for thin films with a Ba concentration of [BaAC]/[MnAC] = 0.4 and higher (not shown here), the α-MnO_2 structure remains stable even after 900°C. Because conversion of the hollandite phase to the insulating Mn_2O_3 phase at moderate temperatures is desired to provide a basis for fault protection in capacitors, thin films with lower Ba concentrations were developed to obtain less thermally stable α-MnO_2. Figure 4 exhibits the XRD pattern of the manganese oxide films with three different Ba concentrations after heat-treatment at 700°C. As shown in Fig. 4, with high Ba acetate concentrations ([BaAC]/[MnAC] = 0.4), a hollandite phase was observed in the thin film samples. However, for ([BaAC]/[MnAC] = 0.1) and ([BaAC]/[MnAC] = 0.04), a phase mixture consisting of hollandite α-MnO_2 and bixbyite Mn_2O_3 was detected.

To optimize the heat-treatment temperature, MnO_2 thin films with low Ba concentrations ([BaAC]/[MnAC] = 0.04) were heat-treated in the temperature range 500°C–850°C. The XRD diffraction patterns of MnO_2 films heat-treated at these different temperatures are shown in Fig. 5. It can be seen there that a very small XRD peak, corresponding to bixbyite phase is found after heat-treatment at 500°C; this peak becomes more intense with higher heat-treatment temperatures. This indicates that conversion of MnO_2 to Mn_2O_3 phase starts around 500°C and the kinetics of this redox reaction increase with increasing temperature, as revealed by enhancement in peak intensity and appearance of additional XRD peaks, assigned to Mn_2O_3 (bixbyite) phase. Thus, for preparation of self-healing MnO_2 electrodes, 550°C was chosen as heat-treatment temperature to ensure that a continuous MnO_2 film is formed through the sintering process without significant growth of the Mn_2O_3 phase.

The change in microstructure with heat-treatment temperature in manganese oxide films with a concentration of [BaAC]/[MnAC] = 0.04 was also observed by scanning electron microscopy. Figure 6 shows the SEM micrographs of manganese oxide films with a concentration of [BaAC]/[MnAC]=0.04 in as-deposited condition and after heat-treatment at 500°C, 700°C, and 900°C. As shown in Fig. 6, the deposited manganese oxide films were smooth and homogeneous; no crack formation was observed. The thin films heat-treated at 500°C shows initial crystallization of MnO_2 hollandite phase, as revealed in GIXRD results. When the annealing temperature was increased to 700°C, the microstructure of manganese oxide films changed into a denser structure. After heat-treatment at 900°C, the film microstructure becomes more dense, with grain growth of the existing particles.

(2) Thin Film Properties

(A) Resistivity of Ba-Doped Thin Films: The electrical properties of the thin films obtained in this study are comparable with that reported for sputtered MnO_2 thin films.[38] Table II summarizes the electrical properties of the Ba-doped manganese oxide films. The temperature dependence of the resistivity between 25°C and 500°C indicates that conduction mechanism exhibits thermally activated behavior in accordance with the well known Arrhenius law:

$$\rho = \rho_o \exp(E_a/kT), \tag{3}$$

where ρ is the resistivity, ρ_o the infinite temperature resistivity, E_a the activation energy, T absolute temperature, and k Boltzmann's constant [Fig. 7(a)]. As shown in Fig. 7(a), all samples showed linear dependence of resistivity on temperature. The activation energies of MnO_2 thin films with different Ba content obtained from Arhenius equation are given in Table II. Differences in activation energies and the corresponding resistivity values were found depending on the initial Ba concentration. Films with a Ba concentration of [BaAC]/[MnAC] = 0.4 are characterized by a low activation energies and resistivity values in the range 0.12 ± 0.08 to 0.24 ± 0.08 eV and 9.8 ± 2, 5.5 ± 1 or 4.2 ± 0.8 Ω·cm, respectively (Table II). The calculated thermal activation

energies are close to that of sputtered MnO_2 film (0.095 eV).[38] The conduction process of MnO_2 is due to carrier hopping between Mn^{3+} and Mn^{4+} ions.[39–44] The low activation energy and resistivity values in the films with a Ba concentration of [BaAC]/[MnAC] = 0.4 are attributed to the stability of hollandite phase at high temperatures, as revealed in GIXRD and high-temperature resistivity results. As shown in Fig. 7(b), for high Ba concentrations the resistivity of the hollandite phase decreases continuously with increasing temperature, which implies that the obtained hollandite structure was stable up to 750°C.

For a moderate Ba concentration ([BaAC]/[MnAC] = 0.1), on the other hand, the resistivity and corresponding activation energy of thin films was around 18.8 ± 4 Ω·cm and 0.31 ± 0.1 eV, respectively, presumably because of the polyphase assemblage of MnO_2 and Mn_2O_3. The hollandite phase transformed to Mn_2O_3 at 675°C, as shown by the resistivity increase in Fig. 7(b). For the lower Ba concentration ([BaAC]/[MnAC] = 0.04), the resistivity and activation energy increased further to 20.2 ± 4 Ω·cm and 0.34 ± 0.1 eV due to an increasing volume fraction of the Mn_2O_3 phase. The phase transition temperature of MnO_2 for low Ba concentration ([BaAC]/[MnAC] = 0.04), was 600°C. The shift in phase transition temperatures with decreasing Ba concentration is consistent with the GIXRD results.

The switching of the hollandite phase to the insulating Mn_2O_3 phase at moderate temperatures is desired to provide a basis for the fault protection of capacitors. Thus, MnO_2 thin films with low Ba concentration ([BaAC]/[MnAC] = 0.04) were prepared and heat-treated at 550°C, and these thin films were further investigated to define their dielectric breakdown behavior, as discussed in the next section.

(B) DC Dielectric Breakdown of Uncoated and MnO_2-Coated Glass Samples: The dielectric breakdown strength of uncoated and MnO_2-coated glass samples was determined at room temperature. After the breakdown, the surfaces of the glass samples were imaged under an optical microscope to reveal the damage generated by dielectric breakdown. The aluminum-coated polypropylene electrodes were also investigated with optical microscopy, after separation from the glass, to determine the electrode area that cleared during the dielectric breakdown. The local heating of electrode material at breakdown site leads to evaporation of electrode material or formation of an insulating phase, which restricts the current flow through defect sites. These evaporated or now insulating electrode regions represent the cleared electrode area. Figure 8 presents the optical microscope images of uncoated and MnO_2-coated glass surfaces and Al electrodes covering the glass. As shown in Fig. 8, in uncoated glass samples, catastrophic breakdown with severe crack formation was observed due to insufficient clearing of the electrode at the fault site during breakdown. For MnO_2-coated glass samples, on the other hand, graceful failure was observed, with very little destruction caused by the dielectric breakdown event and significant electrode clearing. The images in Fig. 8 shows the optical images of the Al top electrodes after the breakdown event. As shown in Fig. 8, the MnO_2 coating improves the electrode area evaporated or cleared during breakdown.

The propensity for self-healing is closely related to the cleared electrode volume during the breakdown process, as described by Eq. (2).[19] When dielectric breakdown occurs, the high current density around the breakdown site will vaporize the electrode and leave a cleared area around the punch-through region. The energy balance of the breakdown process is described by equating the electrostatic energy lost by the capacitor $[C/2(V^2-V_r^2)]$ with the heat required for evaporation (H_e), the heat needed for temperature increase around the breakdown spot (H_s), and the heat gained by redox reactions (H_o). The values, V and V_r are the voltage applied to capacitor and the lowest voltage on single hole breakdown, respectively.[19]

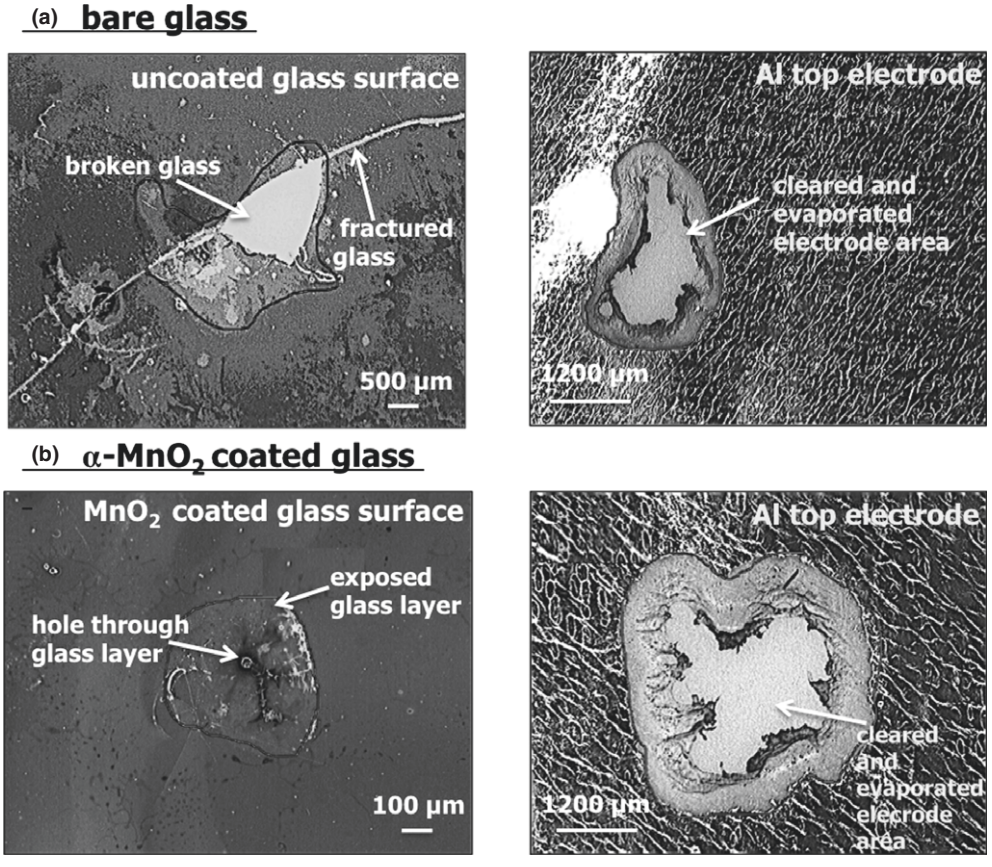

Fig. 8. Optical microscope images of uncoated and MnO_2-coated glass surfaces and Al top electrodes, covering the glass. Catastrophic and graceful dielectric failure modes were observed for uncoated and MnO_2-coated glass samples, respectively.

$$\frac{C}{2}(V^2 - V_r^2) = H_e + H_s - H_o \quad (4)$$

For bare glass samples, when the dielectric breakdown occurs, the electrostatic energy released at fault regions vaporizes the Al electrode around the fault channel. For the MnO_2-coated glass samples, on the other hand, Joule heating released at the breakdown site could also drive a controlled redox reactions between the MnO_2 interlayer and aluminum. The localized heating of MnO_2 electrodes causes conversion of the MnO_2 electrodes, which has a resistivity of 4–5 $\Omega{\cdot}cm^2$ to an insulating Mn_2O_3 phase, having a resistivity of 10^6–10^7 $\Omega{\cdot}cm^2$ (Reaction [1]) so that the current flow through the defect sites are restricted. The removal of conduction sites retards the breakdown of glass, which results in remarkable improvement in dielectric breakdown strength and associated cleared electrode area. In addition, the exothermic reaction and availability of oxygen to the aluminum conductor (Reactions [1] and [2]) promote electrode clearing in MnO_2-coated glass samples.

$$2MnO_2 \xrightarrow{500\sim600^\circ C} Mn_2O_3 + O^* \quad [1]$$

$$2Al + 3O^* \longrightarrow Al_2O_3 \quad [2]$$

The improvement in dielectric breakdown voltage and associated cleared area after coating the glass samples with MnO_2 is shown in Fig. 9. Figure 9(a) depicts the dependence of the cleared electrode area on breakdown voltage for bare and MnO_2-coated glass samples. Figure 9(b) presents the change in energy released at defect sites for bare and MnO_2-coated glass samples. There are several key points that are apparent from these two figures. First, the breakdown voltage and associated cleared electrode area are greatly increased after coating the glass with MnO_2. It was found that the MnO_2 coating improves the breakdown voltage by ~60% relative to uncoated glass substrates. It is believed that the main mechanism responsible for the improvement in both the breakdown voltage and the associated electrode clearing area is controlled redox reactions between the MnO_2 interlayer and aluminum, so that an expanded insulating region, or cleared area, is formed around the breakdown site. The contribution of this extra energy to the total energy released at defect sites after coating with MnO_2 can be seen in Fig. 9(b). Second, the cleared area increases with breakdown voltage because the energy dissipated in the arc is proportional to the applied voltage as shown in Eq. (2).[19] Sassoulas et al. measured the cleared electrode area on polypropylene thin films during the breakdown process and discussed its relation to the breakdown voltage.[45] It was found that the area cleared by a breakdown increased with breakdown voltage and was independent of the thickness of the polypropylene thin film.[45] The results shown in Fig. 9 show a similar trend and the increased slope with MnO_2 is attributed to the additional energy for clearing that is supplied by reduction reaction, which would increase the energy term and vaporization volume on the right side of Eq. (2) for a given breakdown voltage.

To confirm the hypothesis that the retardation of the breakdown process was the result of the phase transformation of the MnO_2 to the more insulating Mn_2O_3 phase (which limits the leakage current at the breakdown site), Raman spectra were acquired. Figure 10 shows Raman spectra of an area near the breakdown site for both bare and MnO_2-coated ([BaAC]/[MnAC] = 0.04) glasses. As shown in Fig. 10(a), Raman bands centered at 440 and 785 cm^{-1} were detected for the bare glass before breakdown. These bands are assigned to SiO_4 tetrahedra with four bridging oxygen ions and six-membered borate ring with one BO_4 tetrahedron, respectively.[46] However, after breakdown, these Raman bands disappeared, and are accompanied by emergence of new bands at 1300 and 1500 cm^{-1}, which corresponds to amorphous C species.[47] Most probably they come from polypropylene which was used as a carrier material for the Al top electrode. Figure 10(b) shows Raman spectra of breakdown region of MnO_2-coated glass before and after breakdown occurs. As shown in Fig. 10(b), Raman bands at 658, 470, and 354 cm^{-1} assigned to the MnO_2 and Mn_2O_3 phases were detected before breakdown occurs.[33] The Raman band corresponding to MnO_2 diminished after breakdown; this was concurrent with a slight increase in the intensity of bands due to Mn_2O_3. This indicates that some of the conducting MnO_2 phase transformed to insulating Mn_2O_3 during the breakdown process.

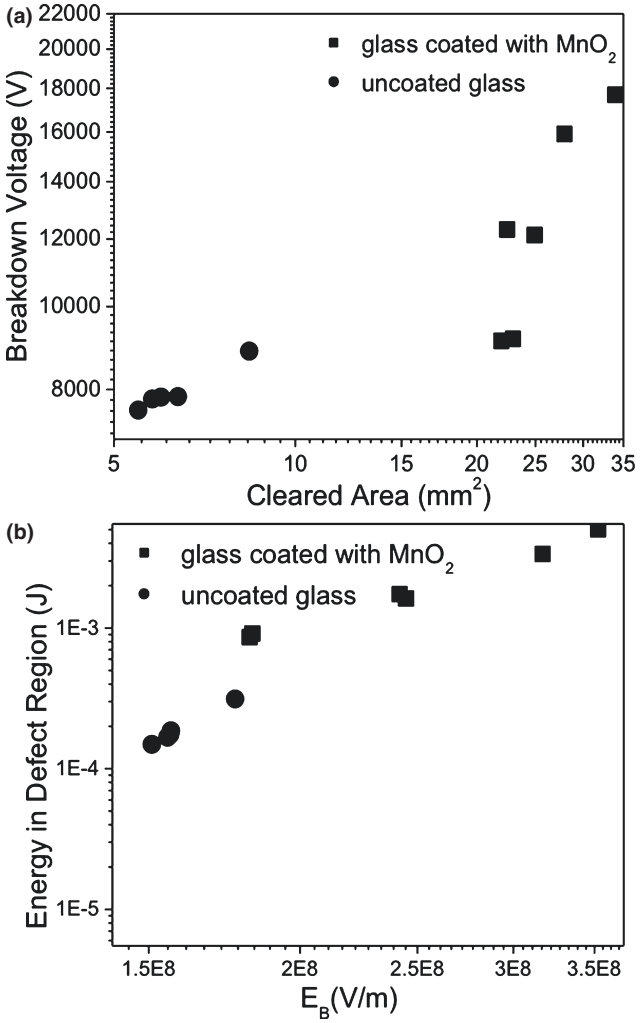

Fig. 9. (a) The dielectric breakdown voltage and corresponding electrode area for uncoated and MnO_2-coated glasses at room temperature, (b) Energy in defect region as a function of breakdown voltage for uncoated and MnO_2-coated glasses at room temperature.

In this study, higher clearing area was observed for MnO_2-coated glass (Fig. 9). It is believed that a controlled redox reaction during breakdown increased the cleared electrode area. The RAMAN results, which show the phase transformation of MnO_2 to Mn_2O_3, are consistent with the dielectric breakdown test results. It was also seen that there is a correlation between dielectric breakdown strength and cleared electrode area. The samples with high breakdown voltage exhibited larger cleared electrode areas.

IV. Conclusions

α-MnO_2 (hollandite) thin films were investigated for their potential as a self-healing electrode in high energy density

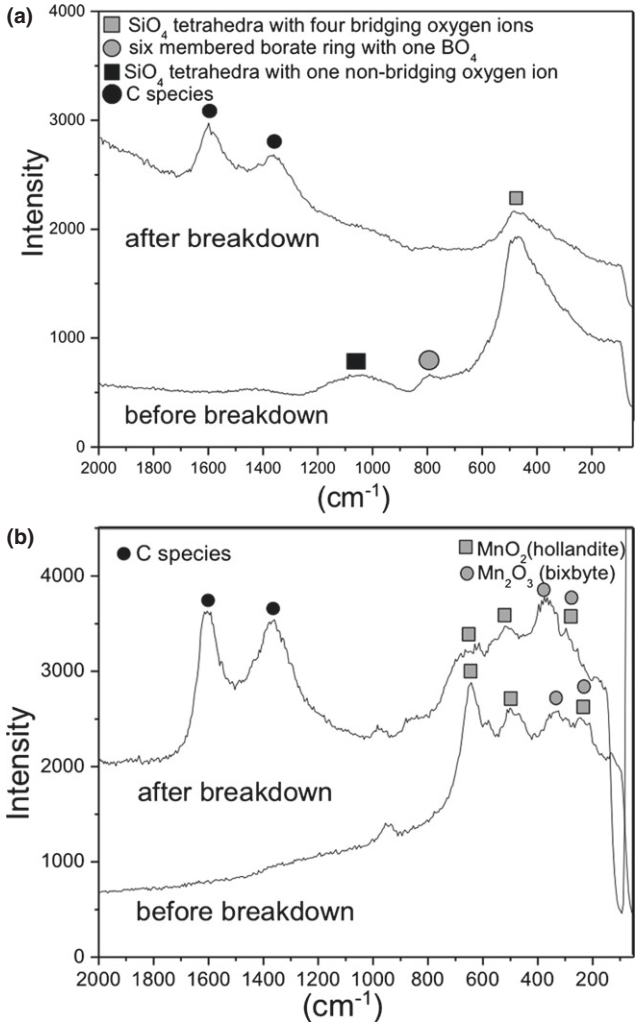

Fig. 10. Raman spectra of breakdown region of (a) bare and (b) MnO_2-coated glass before and after breakdown occurs.

glass capacitor applications. Pure and Ba-doped Mn_xO_y films were prepared via a sol–gel method on a thin boroaluminosilicate glass. It was found that the concentration of Ba affects the crystallization behavior of the Mn_xO_y thin film, with increased Ba concentration resulting in an increased phase stability of α-MnO_2 (hollandite). While pure Mn_xO_y thin films formed Mn_2O_3 (bixbyite), Ba-doped Mn_xO_y thin films crystallized as either pure α-MnO_2 (hollandite) or a phase mixture of α-MnO_2 (hollandite) and α-Mn_2O_3 (bixbyite) depending on the initial Ba concentration. The phase transition temperature of α-MnO_2 (hollandite) to α-Mn_2O_3 (bixbyite) was also found to vary with increased Ba concentration; it was 600°C for BaAC]/[MnAC] = 0.04 and >900°C for BaAC]/[MnAC] = 0.4. Furthermore, Ba-doped MnO_2 thin films (([BaAC]/[MnAC] = 0.4) heat-treated at 550°C were used as a self-healing electrodes for thin boroaluminosilicate glasses. The phase changes from α-MnO_2 (hollandite) to α-Mn_2O_3 (bixbyite) during breakdown, which limits the leakage current at breakdown site, enables boroaluminosilicate glass to sustain higher operating electrical fields. This leads to enhancement in both the dielectric breakdown strength and the associated cleared area of boroaluminosilicate glasses. The self-healing MnO_2 electrodes may be suitable for use in high energy density glass capacitor applications. Extrinsic factors limit the breakdown field in glass. Defects such as pores and cracks create low-field conduction paths that often initiate the breakdown process. The addition of a MnO_2 interlayer between the aluminum conductor and glass dielectric promotes the clearing process and removes the electric field from regions of the extrinsic defects, allowing for an overall higher field to be applied to the capacitor.

Acknowledgments

The authors would like to thank the Center for Dielectrics and Piezoelectrics for funding this research. The authors would also like to thank to Derek Wilke and Jeff Long for their assistance with electrical measurements and thank Dr. Eugene Furman for his helpful discussions on dielectric breakdown.

References

[1]H. Ogihara, C. A. Randall, and S. Trolier-McKinstry, "High-Energy Density Capacitors Utilizing 0.7 $BaTiO_3$–0.3 $BiScO_3$ Ceramics," *J. Am. Ceram. Soc.*, **92**, 1719–24 (2009).

[2]D. P. Shay, N. J. Podraza, N. J. Donnelly, and C. A. Randall, "High Energy Density, High Temperature Capacitors Utilizing Mn-Doped $0.8CaTiO_3$–$0.2CaHfO_3$ Ceramics," *J. Am. Ceram. Soc.*, **95**, 1348–55 (2012).

[3]T. Akiyoshi, G. Wang, H. Hofmann, and M. T. Lanagan, "Ripple Current and Electrical Noise Characterization of DC BUS Capacitors for Future Power Electronics," *Proc. CARTS*, **27**, 159–71 (2007).

[4]G. R. Love, "Energy Storage in Ceramic Dielectrics," *J. Am. Ceram. Soc.*, **73**, 323–8 (1990).

[5]M. P. Manoharan, et al., "Flexible Glass for High Temperature Energy Storage Capacitors," *Energy Technol.* **1**, 313–8 (2013).

[6]K. wa Gachigi, "Electrical Energy Storage in Antiferroelectric-Ferroelectric Phase Switching, Chemically Modified Lead Zirconate Ceramics"; Ph.D. Thesis. The Pennsylvania State University, University Park, Pennsylvania, 1992.

[7]J. Y. Lia, L. Zhang, and S. Ducharme, "Electric Energy Density of Dielectric Nanocomposites," *Appl. Phys. Lett.*, **90**, 132901–3 (2007).

[8]J. H. Tortai, N. Bonifaci, A. Denat, and C. Trassy, "Diagnostic of the Self-Healing of Metallized Polypropylene Film by Modeling of the Broadening Emission Lines of Aluminum Emitted by Plasma Discharge," *J. Appl. Phys.*, **97**, 053304–9 (2005).

[9]M. Rabuffi and G. Picci, "Status Quo and Future Prospects for Metallized Propylene Energy Storage Capacitors," *IEEE Trans. Plasma Sci.*, **30**, 1939–42 (2002).

[10]L. Zhu and Q. Wang, "Novel Ferroelectric Polymers for High Energy Density and Low Loss Dielectrics," *Macromolecules*, **45**, 2937–54 (2012).

[11]M. Domonkos, et al., "Submicrosecond Pulsed Power Capacitors Based on Novel Ceramic Technologies," *IEEE Trans. Plas. Sci.*, **38**, 2686–93 (2010).

[12]G. Brennecka, J. Ihlefeld, J.-P. Maria, B. Tuttle, and P. Clem, "Processing Technologies for High-Permittivity Thin Films in Capacitor Applications," *J. Am. Ceram. Soc.*, **93**, 3935–54 (2010).

[13]T. Murata, P. Dash, E. Furman, C. Pantano, and M. Lanagan, "Electrode-Limited Dielectric Breakdown of Alkali Free Glass," *J. Am. Ceram. Soc.*, **95**, 1915–9 (2012).

[14]N. J. Smith, B. Rangarajan, M. T. Lanagan, and C. G. Pantano, "Alkali-Free Glass as a High Energy Density Dielectric Material," *Mater. Lett.*, **63**, 1245–8 (2009).

[15]H. Lee, N. J. Smith, C. G. Pantano, E. Furman, and M. T. Lanagan, "Dielectric Breakdown of Thinned BaO–Al_2O_3–B_2O_3–SiO_2 Glass," *J. Am. Ceram. Soc.*, **93**, 2346–51 (2010).

[16]J. J. O'Dwyer, *The Theory of Electrical Conduction and Breakdown in Solid Dielectrics*. Oxford University Press, London, 1973.

[17]F. Forlani and N. Minnaja, "Electric Breakdown in Thin Dielectric Films," *J. Vac. Sci. Technol.*, **6**, 518–26 (1969).

[18]R. Gerson and T. C. Marshall, "Dielectric Breakdown of Porous Ceramics," *J. Appl. Phys.*, **30**, 1650–3 (1959).

[19]N. Klein, "The Mechanism of Self-Healing Electrical Breakdown in MOS Structures," *IEEE Trans. Electron Devices*, **13**, 788–805 (1966).

[20]J. Prymak, "New Tantalum Capacitors in Power Supply Applications," *IEEE Industry Appl. Conf., 33rd IAS Annual Meeting*, **v2**, 1129–37 (1998).

[21]D. J. DiMaria, E. Cattier, and D. Arnolda, "Impact Ionization, Trap Creation, Degradation, and Breakdown in Silicon Dioxide Films on Silicon," *J. Appl. Phys.*, **73**, 3367–84 (1993).

[22]N. Klein, *Advances in Electronics and Electron Physics*, pp. 309–424. Academic Press, New York City, New York, 1969.

[23]Y. U. Jeong and A. Manthiram, "Nanocrystalline Manganese Oxides for Electrochemical Capacitors with Neutral Electrolytes," *J. Electrochem. Soc.*, **149**, 1419–22 (2002).

[24]R. N. Reddy and R. G. Reddy, "Sol–Gel MnO_2 as an Electrode Material for Electrochemical Capacitors," *J. Power Sources*, **124**, 330–5 (2003).

[25]D.-K. Kwon, T. Akiyoshi, H. Lee, and M. T. Lanagan, "Synthesis and Electrical Properties of Stabilized Manganese Dioxide (α-MnO_2) Thin-Film Electrodes," *J. Am. Ceram. Soc.*, **91**, 906–9 (2008).

[26]M.-W. Xu and S.-J. Bao, "Nanostructured MnO_2 for Electrochemical Capacitor"; pp. 258–67 in *Energy Storage in the Emerging Era of Smart Grids*, Edited by R. Carbone. InTech, 2011, ISBN: 978-953-307-269-2.

[27]T. Nakamura, R. Tai, T. Nishimura, and K. Tachibana, "Spectroscopic Study on Metallorganic Chemical Vapor Deposition of Manganese Oxide Films," *J. Electrochem. Soc.*, **152**, 584–7 (2005).

[28]S. C. Pang and M. A. Anderson, "Novel Electrode Materials for Electrochemical Capacitors: Part II. Material Characterization of Sol–Gel-Derived and Electrodeposited Manganese Dioxide Thin Films," *J. Mater. Res.*, **15**, 2096–106 (2000).

[29]O. Nilsen, H. Fjellvag, and A. Kjekshus, "Growth of Manganese Oxide Thin Films by Atomic Layer Deposition," *Thin Solid Films*, **444**, 44–51 (2003).
[30]B. Dong, T. Xue, C.-L. Xu, and H.-L. Li, "Electrodeposition of Mesoporous Manganese Dioxide Films from Lyotropic Liquid Crystalline Phases," *Micro. Meso. Mater.*, **112**, 62731 (2008).
[31]R. W. Landorf and S. J. Licht, "Sputtered Manganese Dioxide as Counterelectrodes in Thin Film Capacitors," *J. Electrochem. Soc.*, **119**, 430–3 (1972).
[32]S. Fritsch and A. Navrotsky, "Thermodynamic Properties of Manganese Oxides," *J. Am. Ceram. Soc.* **79**, 1761–8 (1996).
[33]C. M. Julien, M. Massot, and C. Poinsignon, "Lattice Vibrations of Manganese Oxides Part I. Periodic Structures," *Spectrochimica Acta, Part A*, **60**, 689–700 (2004).
[34]S. Wells, *Structural Inorganic Chemistry*, 4th edition, pp. 458. Clarendon Press, Oxford, 1975.
[35]S. Johnson, M. F. Mansuetto, M. M. Thackeray, Y. Shao-Horn, and S. A. Hackney, "Stabilized Alpha-MnO_2 Electrodes for Rechargeable 3V Lithium Batteries," *J. Electrochem. Soc.*, **144**, 2279–83 (1997).
[36]J. B. Goodenough, "Electronic-Structure of CMR Manganites," *J.Appl. Phys.*, **81**, 5330–5 (1997).
[37]Q. I. Feng, Y. Kazumichi, and N. Yamasaki, "Hydrothermal Soft Chemical Process for Synthesis of Manganese Oxides with Tunnel Structures," *J. Porous Mater.*, **5**, 153–61 (1998).
[38]J. P. Fau and A. Rousset, "Electrical Properties of Sputtered MnO_2 Thin Film," *Appl. Surf. Sci.*, **78**, 203–10 (1994).
[39]V. G. Bhide and R. V. Damle, "Dielectric Properties of Manganese Dioxide I, II," *Physica*, **26**, 33–42, 513–519 (1960).
[40]E. Preisler, "Semiconductor Properties of Manganese Dioxide," *J. Appl. Electrochem.*, **6**, 311–20 (1976).
[41]X. Xia, H. Li, and Z.-H. Chen, "The Study of Semiconduction Properties of MnO_2 with Different Degrees of Reduction," *J. Electrochem. Soc.*, **136**, 266–71 (1989).
[42]S. Ishiwata, J. W. G. Bos, Q. Huang, and R. J. Cava, "Structure and Magnetic Properties of Hollandite $Ba_{1.2}Mn_8O_{16}$," *Phys.: Condens. Matter*, **18**, 3745–52 (2006).
[43]P. Umek, et al., "Synthesis of 3D Hierarchical Self-Assembled Microstructures Formed from r-MnO_2 Nanotubes and Their Conducting and Magnetic Properties," *J. Phys. Chem. C*, **113**, 14798–803 (2009).
[44]H. Sato, T. Enoki, J.-I. Yamaura, and N. Yamamoto, "Charge Localization and Successive Magnetic Phase Transitions of Mixed-Valance Manganese Oxides $K_{1.5}(H_3O)_XMn_8O_{16}(0 < X < 0.5)$," *Phys. Rev. B*, **59**, 12836–41 (1999).
[45]P.-O. Sassoulas, B. Gosse, and J.-P. Gosse, "Self-Healing Breakdown of Metallized Polypropylene" *Proc. IEEE 7th Inter. Conf. Solid Dielectr.*, 275–8 (2001).
[46]W. I. Konijnendijk and J. M. Stevels, "The Structure of Borosilicate Glasses Studied by Raman Scattering," *J. Non-Cryst. Sol.*, **20**, 193–224 (1976).
[47]M. Kahn and W. Waldhauser, "Raman Spectroscopy of Carbon Based Films – Spectra Interpretation and Selected Applications," *BHM (Berg- und Hüttenmännische Monatshefte)*, **155**, 534–40 (2010). □